

Figures of merit for detectors in digital radiography. I. Flat background and deterministic blurring

Angel R. Pineda^{a)} and Harrison H. Barrett

University of Arizona, Radiology Research Building 211, 1609 North Warren, Tucson, Arizona 85724

(Received 11 June 2002; accepted for publication 16 October 2003; published 27 January 2004)

Digital radiography systems can be thought of as continuous linear shift-invariant systems followed by sampling. This view, along with the large number of pixels used for flat-panel systems, has motivated much of the work which attempts to extend figures of merit developed for analog systems, in particular noise equivalent quanta (NEQ) and detective quantum efficiency (DQE). A more general approach looks at the system as a continuous-to-discrete mapping and evaluates the signal-to-noise ratio (SNR) completely from the discrete data. In this paper, we study the effect of presampling blur on these figures of merit for a simple model that assumes that the background fluence is constant and that the blurring of the signal is deterministic. We find that for small signals, even in this idealized model, commonly used DQE/NEQ formulations do not accurately track the behavior of the fully digital SNR. Using these NEQ-based figures of merit would lead to different design decisions than using the ideal SNR. This study is meant to bring attention to the assumptions implicitly made when using Fourier methods. © 2004 American Association of Physicists in Medicine. [DOI: 10.1118/1.1631426]

Key words: image quality, detectability, digital radiography, DQE, NEQ

I. INTRODUCTION

Most efforts regarding the evaluation of digital radiography center around noise equivalent quanta (NEQ) and detective quantum efficiency (DQE). These figures of merit combine the digital and continuous aspects of the imaging system.¹⁻⁵ They are an attempt to provide a frequency-dependent figure of merit that can be used to optimize the hardware for the task of signal detection. These NEQ and DQE formulations are being used to make design decisions such as the preferred amount of presampling blur.^{5,6} These studies found that some presampling blur not only reduces aliasing but may also improve the performance of the digital detector.

In analog radiography systems with a stationary and linear shift-invariant (LSIV) model, one can decompose the signal-to-noise (SNR) into the hardware component and an object component.^{7,8} The NEQ gives the hardware-dependent part of SNR. Hence, by optimizing NEQ, one can optimize the hardware without taking into account the object to be imaged. The separation of the object and hardware parts depends on the Fourier transform diagonalizing both the system operator for a LSIV system and the autocovariance function for a wide-sense stationary (WSS) random process. In digital radiography there is no such transformation since the object being imaged is continuous and the data are discrete and finite.

The lack of a single transformation that diagonalizes both the deterministic and stochastic descriptions of the system leads to different formulations for NEQ and DQE. Using a large number of pixels as a surrogate for a continuous representation of the data, one can compute quantities analogous to the noise power spectrum (NPS) and the modulation transfer function (MTF). The purpose of this paper is to compare commonly used formulations of NEQ and DQE to the ideal

SNR (from a detection-theoretic view). In particular, we draw attention to the assumptions implicitly made when using Fourier methods. To this end, we use a simplified model that assumes a flat background and deterministic blurring. In the accompanying paper,⁹ we study the effects of a finite number of secondaries, nonuniform x-ray fluence, and anatomical variation.

II. CONTINUOUS-TO-DISCRETE MODEL

We consider a one-dimensional (1D) linear digital radiography system with deterministic blurring. This imaging system maps the incoming x-ray Poisson point process $u(x)$ to a finite data vector \mathbf{g} . The incoming x-ray point process $u(x)$ is given by

$$u(x) = \sum_{j=1}^J \delta(x - x_j), \quad (1)$$

where J is the Poisson-distributed number of x rays and $\{x_j\}$ are the locations of the randomly distributed x rays with a fluence of $f(x)$, i.e., $\langle u(x) \rangle = f(x)$. In the absence of electronic noise, the imaging system can be written as

$$g_m = \sum_{j=1}^J h_m(x_j) = \int_{-\infty}^{\infty} h_m(x) f(x) dx + n_m, \quad (2)$$

where g_m is the measurement at the m th pixel, $h_m(x)$ is the sensitivity function of the m th pixel, and the noise at each pixel, n_m , is defined by

$$n_m \equiv g_m - \int_{-\infty}^{\infty} h_m(x) f(x) dx. \quad (3)$$

Written in vector form, Eq. (2) becomes $\mathbf{g} = [\mathcal{H}_{\text{cd}}\mathbf{f}] + \mathbf{n}$, where \mathcal{H}_{cd} is the continuous-to-discrete operator which gives the noise-free measurement

$$\bar{g}_m = [\mathcal{H}_{\text{cd}}f]_m = \int_{-\infty}^{\infty} h_m(x)f(x)dx. \quad (4)$$

For the purpose of presenting the various figures of merit, we write the continuous-to-discrete map as a continuous-to-continuous map followed by point sampling. Furthermore, we consider a shift-invariant continuous (presampling) map,

$$g_{\text{ps}}(x) = \sum_{j=1}^J h(x-x') = \int_{-\infty}^{\infty} h(x-x')f(x')dx' + n_{\text{ps}}(x), \quad (5)$$

where $g_{\text{ps}}(x)$ is the presampling data random process, $h(x-x')$ is the kernel of the continuous-to-continuous map,

$$[\mathcal{H}_{\text{cc}}f](x) = \int_{-\infty}^{\infty} h(x-x')f(x')dx', \quad (6)$$

and n_{ps} is defined as in the continuous-to-discrete case:

$$n_{\text{ps}}(x) \equiv g_{\text{ps}}(x) - \int_{-\infty}^{\infty} h(x-x')f(x')dx'. \quad (7)$$

The data before sampling is a sum of sensitivity functions whose locations are uniformly random. The statistics of this random process will depend on the number of x rays and the shape of the sensitivity functions.¹⁰ As is customary in the literature connecting DQE with signal detectability,^{7,11,12} we model the data before sampling as a Gaussian random process. This model is justified by the central limit theorem if the mean number of photons per pixel is reasonably large.

The continuous-to-discrete map is obtained by point sampling and adding electronic noise n_{elec} ,

$$\begin{aligned} g_m &= \int_{-\infty}^{\infty} \delta(x_m - x)g_{\text{ps}}(x)dx + [n_{\text{elec}}]_m \\ &= g_{\text{ps}}(x_m) + [n_{\text{elec}}]_m. \end{aligned} \quad (8)$$

To simplify the notation and our computations, we let the unit of distance be the pixel pitch ($x_m = m$ pixels). With respect to our original description of the continuous-to-discrete mapping we have $h_m(x) = h(m-x)$, and $n_m = n_{\text{ps}}(m) + [n_{\text{elec}}]_m$.

In this paper, we let the incoming background x-ray Poisson process $u(x)$ have a constant fluence. Given a constant fluence, $\langle u(x) \rangle = b_0$, the autocorrelation of $u(x)$ is given by

$$\langle (u(x) - b_0)(u(x') - b_0) \rangle = b_0 \delta(x - x'). \quad (9)$$

We also assume the electronic noise has mean zero, is uncorrelated across pixels, and has the same variance (σ_n^2) at all pixels. Under these conditions, the data covariance matrix elements are¹³

$$\begin{aligned} &\langle (g_m - \bar{g}_m)(g_{m'} - \bar{g}_{m'}) \rangle \\ &= \int_{-\infty}^{\infty} dx h_m(x) \int_{-\infty}^{\infty} h_{m'}(x') b_0 \delta(x - x') dx' + \sigma_n^2 \delta_{mm'} \\ &= b_0 \int_{-\infty}^{\infty} h_m(x) h_{m'}(x) dx + \sigma_n^2 \delta_{mm'}. \end{aligned} \quad (10)$$

In the accompanying paper,⁹ we consider more realistic situations.

III. FIGURES OF MERIT FOR THE CONTINUOUS MAP

We begin by considering the map from the x-ray point process to the presampling data random process. For that imaging system, the detection task can be phrased as discriminating between the following two hypotheses:

$$g_{\text{ps},0}(x) = [\mathcal{H}_{\text{cc}}b](x) + n_{\text{ps}}(x) \quad \text{signal absent}, \quad (11)$$

$$g_{\text{ps},1}(x) = [\mathcal{H}_{\text{cc}}b](x) + [\mathcal{H}_{\text{cc}}s](x) + n_{\text{ps}}(x) \quad \text{signal present},$$

where $g_{\text{ps},i}(x)$ represents the data before sampling under the i th hypothesis, $b(x)$ is the background x-ray fluence, and $s(x)$ is the signal x-ray fluence.

For the following analysis, the background is fixed and constant [$b(x) = b_0$] and the signal is deterministic, low contrast, and known, in other words, we consider the signal-known-exactly/background-known-exactly (SKE/BKE) detection task where the signal does not affect the data statistics. We model the data before sampling as a Gaussian random process with the following autocovariance function:

$$\begin{aligned} \langle (g_{\text{ps}}(x) - \bar{g}_{\text{ps}})(g_{\text{ps}}(x') - \bar{g}_{\text{ps}}) \rangle &= \langle n_{\text{ps}}(x)n_{\text{ps}}(x') \rangle \\ &= k_{\text{ps}}(x, x'). \end{aligned} \quad (12)$$

The ideal observer chosen by the Neyman–Pearson criterion requires that the observer maximize the true positive fraction for any false positive fraction in a detection task.¹⁴ Therefore, it optimizes the area under the receiver operating characteristic curve (AUC). The ideal observer according to the Neyman–Pearson criterion is¹⁵

$$t_{\text{ideal}}(g_{\text{ps}}(x)) = \int_{-\infty}^{\infty} dx [\mathcal{H}_{\text{cc}}s](x) \int_{-\infty}^{\infty} dx' k_{\text{ps}}^{-1}(x, x') g_{\text{ps}}(x'), \quad (13)$$

where $k_{\text{ps}}^{-1}(x, x')$ is the kernel of the inverse of the autocovariance operator, defined such that

$$\int_{-\infty}^{\infty} dx k_{\text{ps}}^{-1}(x, x') \int_{-\infty}^{\infty} du k_{\text{ps}}(x', u) f(u) = f(x). \quad (14)$$

The SNR for any test statistic (t) is defined as

$$\text{SNR}_t = \frac{\langle t_1 \rangle - \langle t_0 \rangle}{\sigma(t)}, \quad (15)$$

where $\langle t_i \rangle$ is the ensemble average under the i th hypothesis and $\sigma(t)$ is the standard deviation of the test statistic. For a Gaussian test statistic (as in this case), the AUC for the de-

tection task is a monotonic transformation of SNR.¹⁶ Therefore we can use SNR to quantify the performance of the ideal observer in an AUC sense.

The SNR² of the ideal observer is given by

$$\text{SNR}_{\text{ideal}}^2 = \int_{-\infty}^{\infty} dx [\mathcal{H}_{\text{cc}s}](x) \int_{-\infty}^{\infty} dx' k_{\text{ps}}^{-1}(x, x') [\mathcal{H}_{\text{cc}s}](x'). \quad (16)$$

A shift-invariant imaging operator is diagonalized by the Fourier transform:

$$\mathcal{F}\{\mathcal{H}_{\text{cc}s}\}(x) = \text{PSTF}(\nu) S(\nu), \quad (17)$$

where \mathcal{F} is the continuous Fourier transform, ν is the frequency variable, $\text{PSTF}(\nu)$ is the presampling transfer function, and $S(\nu)$ is the Fourier transform of the signal. For a WSS random process [$k_g(x, x') = k_g(x - x')$], the Fourier transform also diagonalizes the inverse of the autocovariance operator, so

$$\mathcal{F}\left\{\int_{-\infty}^{\infty} dx' k_{\text{ps}}^{-1}(x - x') s(x')\right\} = \frac{S(\nu)}{\text{NPS}(\nu)}, \quad (18)$$

where $\text{NPS}(\nu)$ is the noise power (Wiener) spectrum defined as the Fourier transform of the autocovariance function:

$$\text{NPS}(\nu) = \mathcal{F}\{k_{\text{ps}}(\Delta x)\}. \quad (19)$$

If we represent the data using the Fourier basis,

$$\mathcal{H}s(x) = \int_{-\infty}^{\infty} d\nu \text{PSTF}(\nu) S(\nu) e^{2\pi i x \nu}, \quad (20)$$

SNR² reduces to

$$\text{SNR}_{\text{ideal}}^2 = \int_{-\infty}^{\infty} d\nu \frac{|\text{PSTF}(\nu)|^2}{\text{NPS}(\nu)} |S(\nu)|^2. \quad (21)$$

At this point we already achieved a separation of the hardware component from the object component in the SNR² expression. By optimizing $|\text{PSTF}(\nu)|^2/\text{NPS}(\nu)$, which can be computed from a characterization of the hardware, we optimize the detectability of any signal. This separation of the hardware and the object of interest avoids having an object-dependent figure of merit. To present the results in a manner that is standard in the community for image quality in digital radiography, we write the signal as a fraction of the background

$$s(x) = b_0 s_0(x), \quad (22)$$

where $s_0(x)$ is a fractional signal. We also phrase the transfer function in terms of the presampling MTF, PSMTF [letting $\text{PSTF}(0) = G$],

$$|\text{PSTF}(\nu)| = G \text{PSMTF}(\nu), \quad (23)$$

leading to the following expression for SNR²:

$$\text{SNR}_{\text{ideal}}^2 = \int_{-\infty}^{\infty} d\nu \frac{b_0^2 G^2 \text{PSMTF}^2(\nu)}{\text{NPS}(\nu)} |S_0(\nu)|^2. \quad (24)$$

Using this notation we can write NEQ¹ (in the cited text, the notation for b_0 is \bar{q}) as

$$\text{NEQ}(\nu) = \frac{b_0^2 G^2 \text{PSMTF}^2(\nu)}{\text{NPS}(\nu)}. \quad (25)$$

This version of NEQ has a maximum (for a quantum-limited system) of b_0 . The DQE is NEQ normalized by NEQ of a quantum limited imaging system,

$$\text{DQE}(\nu) = \frac{\text{NEQ}(\nu)}{b_0}. \quad (26)$$

The NEQ and DQE are frequency-dependent figures of merit that do not depend on the object characteristics. If one optimizes NEQ or DQE at all frequencies, the system has been optimized for all objects in a SKE/BKE detection task for a system with continuous data that is WSS and LSIV. These properties of NEQ and DQE made them popular and useful in analyzing continuous radiography systems.

IV. FIGURES OF MERIT FOR DIGITAL RADIOGRAPHY

In digital radiography we have a digital detector that, while it has a large number of pixels, still provides a discrete representation of the data. Each of the approaches to follow will attempt to generalize the figures of merit from continuous radiography to this new setting.

A. The Hotelling approach

If we do not attempt to model the process that leads to the digital data, the task can be seen as discriminating between the following two hypotheses:¹⁷⁻¹⁹

$$\mathbf{g}_0 = \mathbf{g}_b + \mathbf{n}, \quad \mathbf{g}_1 = \mathbf{g}_b + \mathbf{g}_s + \mathbf{n}, \quad (27)$$

where \mathbf{g}_i is a finite array of measurements under the i th hypothesis, and \mathbf{g}_b and \mathbf{g}_s are the components of the measurement arising from the background and signal, respectively, and \mathbf{n} is the noise. Just as in the continuous case, we pose the task as the SKE/BKE detection task with a low-contrast signal.

For data with Gaussian statistics, the ideal observer by the Neyman–Pearson criterion is the Hotelling test statistic,^{12,20}

$$t_{\text{ideal}}(\mathbf{g}) = \mathbf{g}_s^t \mathbf{K}_g^{-1} \mathbf{g}, \quad (28)$$

where \mathbf{g}_s^t is the transpose of the signal in the data and \mathbf{K}_g^{-1} is the inverse of the data covariance matrix. The SNR² for this test statistic is given by

$$\text{SNR}^2(\text{ideal}) = \mathbf{g}_s^t \mathbf{K}_g^{-1} \mathbf{g}_s. \quad (29)$$

This is the discrete data analog of the SNR expression in the continuous case shown in Eq. (16). At this point, we have assumed that the measurements are Gaussian distributed but there are no shift-invariance or stationarity assumptions.

The signal \mathbf{g}_s depends on the location (l) of the signal and therefore so does SNR. To obtain an SNR that is independent of location, we average over signals uniformly distributed over a pixel⁸

$$\langle \text{SNR}^2(\text{ideal}) \rangle_{\text{loc}} = \int_{-1/2}^{1/2} dl \text{SNR}^2(\text{ideal}, l). \quad (30)$$

For discrete data with Gaussian statistics, the Hotelling observer is rigorously ideal by several criteria including: the Neyman–Pearson criterion,^{12,14} maximizing SNR_t ,²⁰ and maximizing the AUC for the detection task.¹⁶ For the imaging situations described in this paper, a Gaussian model describes the data statistics well. For that reason, we label SNR of the Hotelling observer as the ideal SNR. In the accompanying paper,⁹ we consider situations (random backgrounds) where the Hotelling observer is not ideal in the Neyman–Pearson sense but still maximizes SNR, and the AUC among linear observers.

B. The DSFT approach

To present the DSFT approach,^{13,21} we consider the limit of a detector with a large number of pixels. The discrete-space Fourier transform (DSFT) is the continuous Fourier transform of a sampled function. Unlike the discrete Fourier transform (DFT), the DSFT can be evaluated for any frequency (θ). We define the DSFT of an infinite-dimensional data vector \mathbf{g} by

$$G^{\text{DSFT}}(\theta) \equiv \sum_{m=-\infty}^{\infty} g_m e^{-2\pi i m \theta}. \quad (31)$$

For a constant background and deterministic blur, the covariance matrix is an infinite-dimensional Toeplitz matrix, satisfying

$$\begin{aligned} [\mathbf{K}_g]_{mm'} &= b_0 \int_{-\infty}^{\infty} h(m-x)h(m'-x)dx + \sigma_n^2 \delta_{mm'} \\ &= b_0 \int_{-\infty}^{\infty} h(v-(m'-m))h(v)dv + \sigma_n^2 \delta_{mm'} \\ &= k_{m'-m}, \end{aligned} \quad (32)$$

with

$$k_l \equiv b_0 \int_{-\infty}^{\infty} h(v-l)h(v)dv + \sigma_n^2 \delta_{l,0}. \quad (33)$$

A key result in writing $\text{SNR}^2(\text{ideal})$ expression using the DSFT is that the infinite vector Ψ with elements $\{\Psi_m = e^{2\pi i \theta m}\}$ is an eigenvector of the data covariance matrix:

$$\begin{aligned} [\mathbf{K}_g \Psi]_m &= \sum_{m'=-\infty}^{\infty} k_{m'-m} e^{2\pi i \theta m'} = e^{2\pi i \theta m} \sum_{l=-\infty}^{\infty} k_l e^{-2\pi i \theta l} \\ &= K^{\text{DSFT}}(\theta) \Psi_m. \end{aligned} \quad (34)$$

In other words, the DSFT diagonalizes the data covariance matrix. Using the above-shown diagonalization, one can write the $\text{SNR}^2(\text{ideal})$ expression for an infinite detector using the DSFT of the signal in the data,^{13,21}

$$\mathbf{g}_s^t \mathbf{K}_g^{-1} \mathbf{g}_s = \int_{-1/2}^{1/2} d\theta \frac{|G_s^{\text{DSFT}}(\theta)|^2}{K^{\text{DSFT}}(\theta)}.$$

To obtain a figure of merit that does not depend on the location (l) of the signal, we average the signal location over a pixel just as we did in the Hotelling case:

$$\begin{aligned} \langle \text{SNR}^2 \rangle_{\text{loc}} &= \int_{-1/2}^{1/2} dl \int_{-1/2}^{1/2} d\theta \frac{|G_s^{\text{DSFT}}(\theta; l)|^2}{K^{\text{DSFT}}(\theta)} \\ &= \int_{-1/2}^{1/2} d\theta \frac{\int_{-1/2}^{1/2} dl |G_s^{\text{DSFT}}(\theta; l)|^2}{K^{\text{DSFT}}(\theta)}, \end{aligned} \quad (35)$$

where we made explicit the dependence of $G_s^{\text{DSFT}}(\theta)$ on the signal location by using the notation $G_s^{\text{DSFT}}(\theta; l)$.

We can write $G_s^{\text{DSFT}}(\theta; l)$ in terms of the continuous Fourier transforms of $s(x)$ and $h(x)$:^{13,21}

$$G_s^{\text{DSFT}}(\theta; l) = \sum_{m=-\infty}^{\infty} H(\theta+m)S(\theta+m)e^{2\pi i m l}, \quad (36)$$

leading to^{8,21}

$$\int_{-1/2}^{1/2} dl |G_s^{\text{DSFT}}(\theta; l)|^2 = \sum_{m=-\infty}^{\infty} |H(\theta+m)|^2 |S(\theta+m)|^2. \quad (37)$$

We then use the periodicity of the DSFT [$K^{\text{DSFT}}(\theta) = K^{\text{DSFT}}(\theta+m)$] to rewrite the expression for $\langle \text{SNR}^2 \rangle_{\text{loc}}$ as

$$\begin{aligned} \langle \text{SNR}^2 \rangle_{\text{loc}} &= \int_{-1/2}^{1/2} d\theta \sum_{m=-\infty}^{\infty} \frac{|H(\theta+m)|^2}{K^{\text{DSFT}}(\theta+m)} |S(\theta+m)|^2 \\ &= \sum_{m=-\infty}^{\infty} \int_{m-1/2}^{m+1/2} d\nu \frac{|H(\nu)|^2}{K^{\text{DSFT}}(\nu)} |S(\nu)|^2 \\ &= \int_{-\infty}^{\infty} d\nu \frac{|H(\nu)|^2}{K^{\text{DSFT}}(\nu)} |S(\nu)|^2, \end{aligned} \quad (38)$$

where the last step follows from breaking up the integral over the entire real axis over integer intervals. Here we have achieved the same type of separation that we saw in continuous radiography but with location averaging and an infinite detector. Note, however, that Eq. (38) involves two distinct kinds of Fourier transform: $H(\nu)$ is the usual Fourier integral, but $K^{\text{DSFT}}(\nu)$ is, of course, a DSFT.

C. The DFT approach

The theory behind this approach¹ is based on using the data from an infinite detector to estimate $g_{\text{ps}}(x)$:

$$\begin{aligned} g_{\text{ps}}(x) &\approx \sum_{m=-\infty}^{\infty} g_m \text{sinc}(x-m) \\ &= \sum_{m=-\infty}^{\infty} g_{\text{ps}}(m) \delta(x-m) * \text{sinc}(x) \\ &+ \sum_{m=-\infty}^{\infty} [n_{\text{elec}}]_m \text{sinc}(x-m) \equiv \hat{g}_{\text{ps}}(x). \end{aligned} \quad (39)$$

This approximation is exact in the absence of electronic noise if $g_{\text{ps}}(x)$ is band-limited below half the sampling frequency. The noise power spectrum is computed for $\hat{g}_{\text{ps}}(x)$ as

$$\begin{aligned} \text{NPS}_{\hat{g}_{\text{ps}}}(\nu) &= \left[\text{NPS}(\nu) * \sum_{m=-\infty}^{\infty} \delta(\nu - m) + \sigma_n^2 \right] \text{rect}(\nu) \\ &\equiv \text{NPS}_{\text{dig}}(\nu). \end{aligned} \quad (40)$$

In practice, NPS_{dig} is estimated using the variance of the DFT coefficients of the data. The numerator in the digital NEQ is the same as in the presampling case but restricts the frequencies to be within those that can be estimated from sample images without aliasing. The denominator replaces the NPS from the presampling data g_{ps} with the NPS of the estimate \hat{g}_{ps} as¹

$$\text{NEQ}_{\text{dig}}(\nu) \equiv \frac{b_0^2 G^2 \text{PSMTF}^2(\nu)}{\text{NPS}_{\text{dig}}(\nu)}. \quad (41)$$

Using this definition of NEQ_{dig} as a building block, we can define a DQE_{dig} ,

$$\text{DQE}_{\text{dig}}(\nu) \equiv \frac{\text{NEQ}_{\text{dig}}(\nu)}{b_0}. \quad (42)$$

The DFT approach for extending the formulation of NEQ and DQE to digital radiography did not start from a detection-theoretic interpretation of these quantities. The NEQ_{dig} and DQE_{dig} were formulated as characterizations of the detector that somehow took into account the resolution and the noise of the system. For a derivation of the circumstances where the DFT approach coincides with the detection-theoretic interpretation, see Appendix A.

V. MODEL USED FOR SIMULATION

To compare the behavior of the different figures of merit we need to specify the details of our 1D model. The sensitivity functions are given by the convolution of the pixel $w_m(x)$ with the presampling blur:

$$h_m(x) = \int_{-\infty}^{\infty} \text{blur}(x - x'; \sigma_b) w_m(x') dx'. \quad (43)$$

For our simulations, we let $w_m(x) = \text{rect}(x - m)$ and

$$\text{blur}(x; \sigma_b) = \frac{1}{\sqrt{2\pi}\sigma_b} \exp\left(-\frac{x^2}{2\sigma_b^2}\right), \quad (44)$$

where x is the continuous space variable (in units of pixels) and σ_b is the blur width. For a schematic of the model, see Fig. 1.

The signals of interest will be modeled by changes in the fluence:

$$s(x; \sigma_s, l, b_0) = C_s(\sigma_s, b_0) \exp\left(-\frac{(x-l)^2}{2\sigma_s^2}\right), \quad (45)$$

where $C_s(\sigma_s, b_0)$ is given by

$$C_s(\sigma_s, b_0) = \left(\frac{b_0}{\sqrt{\pi}\sigma_s}\right)^{1/2}. \quad (46)$$

This normalization of the signal sets the input SNR equal to 1 as in Ref. 19.

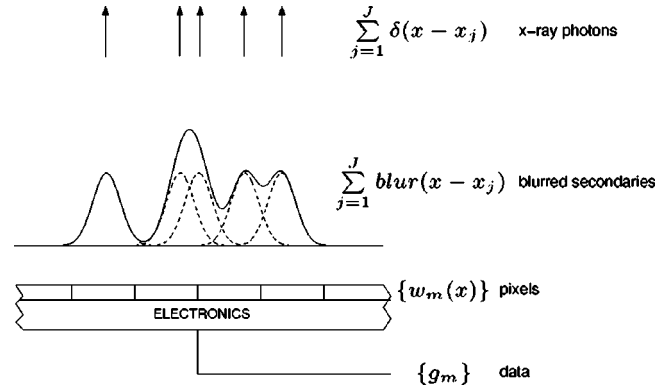


Fig. 1. Schematic of the model used for simulation. We consider the case of a uniform background fluence and deterministic blurring of the x rays.

In our simulations l varied within the center pixel in 0.01 pixel increments, b_0 was kept constant at 10^6 x-ray photons per pixel, and the detector size was 256 pixels. When we refer to adding 10% electronic noise, we mean that σ_n^2 is equal to $0.1b_0$. This is equivalent to adding 10% of the variance in the case with no blurring and no electronic noise. Using this model we compute all NEQ-inspired SNRs as well as the ideal-observer SNR.

VI. COMPUTATION OF THE FIGURES OF MERIT

Computation of the figures of merit will assume that we can estimate the PSMTF and the covariance matrix from a set of sample images. While estimating these quantities will lead to errors, for the purposes of this paper we will use the exact PSMTF and covariance matrix.

System optimization requires a scalar figure of merit. For this reason, we will restrict our comparison to the location-averaged versions of the SNR^2 for the Hotelling and DSFT approaches. For the DFT approach, we use $\text{NEQ}_{\text{dig}}(\nu)$ to compute a SNR^2 .

To create a SNR^2 from $\text{NEQ}_{\text{dig}}(\nu)$, we begin by computing $\text{NPS}_{\text{dig}}(\nu)$ from the data covariance matrix:

$$\text{NPS}_{\text{dig}}(\nu_m) \equiv [\mathbf{DK}_g\mathbf{D}^\dagger]_{mm} = [\mathbf{K}_{\text{DFT}}]_{mm}, \quad (47)$$

where \mathbf{K}_{DFT} is the covariance matrix of the DFT coefficients and \mathbf{D} is the matrix representation of the unitary DFT:

$$[\mathbf{D}\mathbf{g}]_k = \frac{1}{\sqrt{M}} \sum_{m=1}^M g_m e^{2\pi i m k / M}, \quad (48)$$

where M is the total number of pixels. Theoretically, $\text{NPS}_{\text{dig}}(\nu)$ is defined for an infinite detector.^{1,21} In practice, it is estimated by averaging periodograms of finite detectors. The above-given expression in terms of the variance of the DFT coefficients is equivalent to averaging an infinite number of periodograms.⁴

Using NPS_{dig} we can define a SNR^2 based on NEQ_{dig} by

$$\text{SNR}^2(\text{DFT}, S_0) = \sum_{\nu_m = -1/2}^{1/2 - 1/M} \text{NEQ}_{\text{dig}}(\nu_m) |S_0(\nu_m)|^2. \quad (49)$$

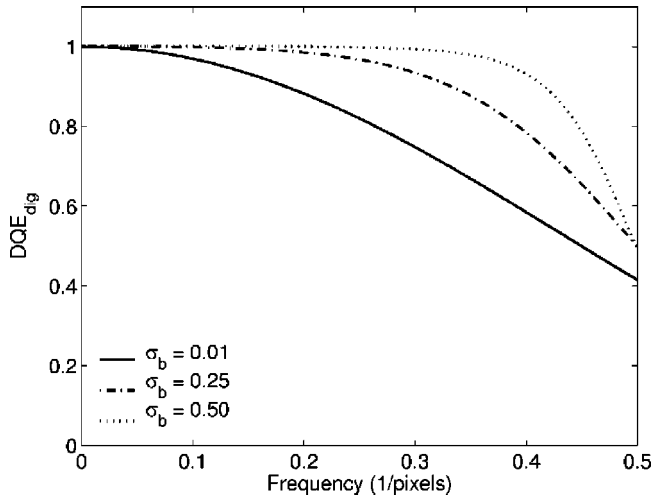


FIG. 2. DQE_{dig} for the model with no pixel gap and no electronic noise. The DQE_{dig} defined using the PSMTF and the DFT can improve as we increase the presampling blur, reproducing qualitatively the result found theoretically and experimentally by Rowland's *et al.* (Ref. 6). We will show that improvements in DQE_{dig} can be a misleading indication of improvement in detector performance.

This figure of merit is not location dependent since it approximates SNR^2 before sampling (see Appendix A).

For the DSFT approach we approximate the DSFT by using the DFT and use the periodicity of the DSFT,

$$K^{\text{DSFT}}(\nu_m + aM) \approx [K_{\text{DFT}}]_{mm} \quad (50)$$

for any integer a . Then we discretize the location-averaged SNR^2 given in Eq. (38) as

$$SNR^2(\text{DSFT}, S_0) = \sum_{\nu_m = -\infty}^{\infty} \frac{b_0^2 |H(\nu_m)|^2}{K^{\text{DSFT}}(\nu_m)} |S_0(\nu_m)|^2 \quad (51)$$

$$= \sum_{\nu_m = -\infty}^{\infty} \text{NEQ}_{\text{dig}}(\nu_m) |S_0(\nu_m)|^2. \quad (52)$$

In our simulations, the DFT was replicated over 20 periods.

For the Hotelling approach, we can compute $SNR^2(\text{ideal})$ without using the continuous description of the presampling system. To approximate the location-averaged version of SNR we use

$$\langle SNR^2(\text{ideal}) \rangle_{\text{loc}} = \frac{1}{N_L} \sum_{l=1}^{N_L} SNR^2(\text{ideal}, l_i) \quad (53)$$

with $N_L = 100$ and l varying from 0.005 to 0.995 (uniformly over the pixel in the center of the array).

VII. SIMULATION RESULTS

The different figures of merit were studied by looking at the effect of varying the amount of presampling blur in a similar way as Rowlands *et al.*⁶ Just as in the Rowlands' paper, we see an improvement in the DFT $DQE_{\text{dig}}(\nu)$ when we look at the case without electronic noise (Fig. 2). Such a result may be interpreted as saying that adding presampling

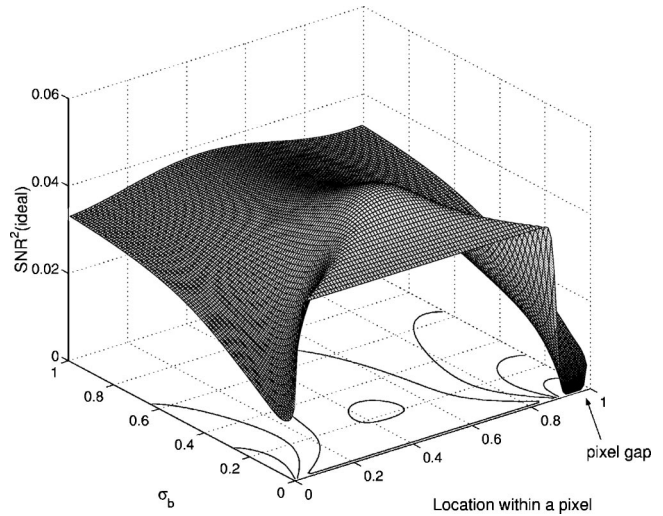


FIG. 3. Dependence of the ideal SNR on presampling blur and object location for a small signal ($\sigma_s = 0.01$ pixels). In this model there is no electronic noise and a pixel gap of 0.1 pixels. The location of the signal with respect to the pixel strongly affects the dependence on presampling blur. A signal in the middle of a pixel has a maximum (along the blur axis) while a signal at the edge monotonically increases. We also see that presampling blur reduces the effect of the interpixel gap.

blur is not only better at reducing aliasing but also at improving overall system performance. This conclusion would be an incomplete version of the story.

We begin by looking at the dependence of $SNR(\text{ideal})$ on the signal location. For signals much smaller than a pixel, we see a strong dependence on location as we vary presampling blur (see Fig. 3). For signals larger than a pixel, we do not see much change.¹⁷ This spatial dependence is important in terms of interpreting the results from detectability computations. In the surface plot (Fig. 3), if we fix the signal location to be in the center of the pixel, there is a maximum along the blur axis. If a detectability study were done with a small signal always at the center of the pixel, the conclusion would be that some presampling blur would significantly improve detectability. The gap shown in Fig. 3 becomes less noticeable as the presampling blur increases. As one would expect, presampling blur takes small signals in the gap and extends them to the active area of the detector.

The NPS_{dig} computations use the variance of the DFT elements but ignore the off-diagonal elements of K_{DFT} . With no electronic noise and $\sigma_b = 1$ pixel, the diagonal elements dominate but the off-diagonal elements are not zero (Fig. 4). The off-diagonal terms are small with respect to the diagonal terms but there are many of them ($\sim N^2$). The error that arises from these off-diagonal terms can be assessed by their effect on signal detectability.

In order to carry out the comparisons between the ideal SNR and NEQ_{dig} , we vary the amount of presampling blur and see how SNRs change (Fig. 5). We find that for small amounts of presampling blur, the DSFT SNR given by Eq. (38) closely approximates the location-averaged ideal SNR ($\langle SNR^2(\text{ideal}) \rangle_{\text{loc}}$).²¹ The difference seen at higher presampling blurs reflects the errors in approximating the DSFT by using the DFT. For our simple model, in the limit of an

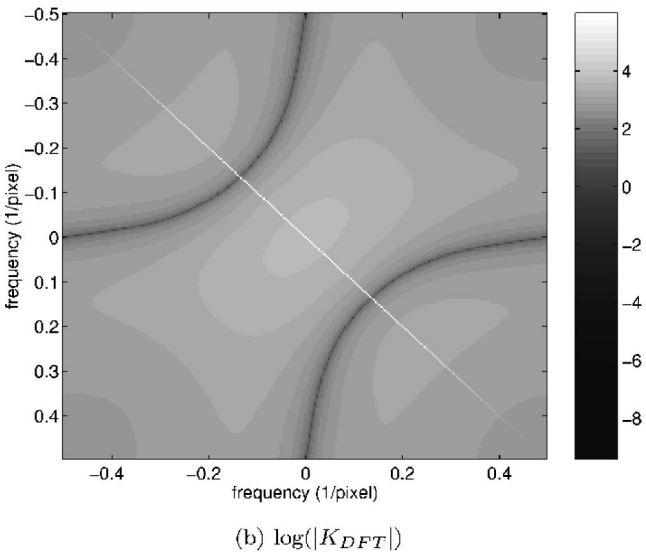
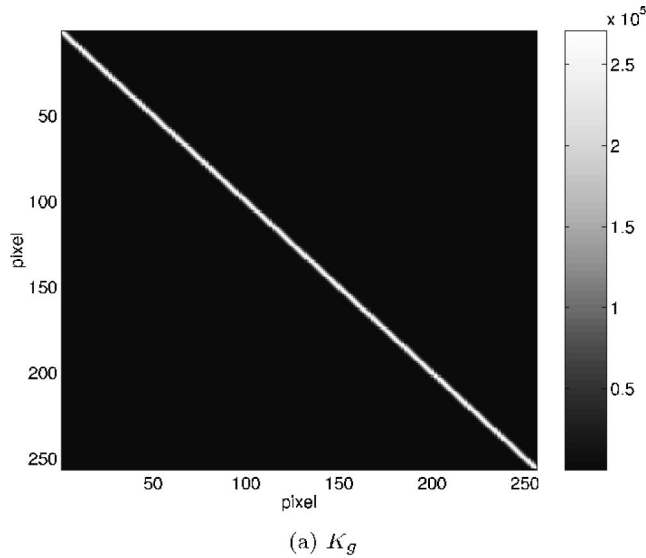


FIG. 4. (a) Covariance matrix of data for $\sigma_b=1.0$ pixel. (b) Log of the covariance matrix of the DFT coefficients of data for $\sigma_b=1.0$ pixel. These covariance matrices show the existence of off-diagonal elements in the covariance matrix of the DFT of the data. Their magnitude is small but there are $\sim N^2$ of them. Their importance will be quantified by their effect on signal detectability.

infinite number of pixels, the Toeplitz covariance matrix becomes circulant.^{13,17}

The DSFT SNR is the only NEQ-based SNR that attempts an explicit connection to signal detectability.²¹ The DFT SNR and DQE(0) should not be compared in terms of their exact agreement with $\langle \text{SNR}^2(\text{ideal}) \rangle_{\text{loc}}$ but in terms of the design decisions to which they lead. In particular, if we look at the case with Poisson noise and no electronic noise with a small signal (Fig. 5), all three SNRs have different behavior as we increase the presampling blur. Part of the motivation for this work was the counterintuitive result found by Rowlands *et al.*⁶ where presampling blur appeared to improve detector performance. This result as seen before in DQE (Fig. 2) is reproduced by our model. The DFT SNR for a small signal has a maximum as we increase presampling

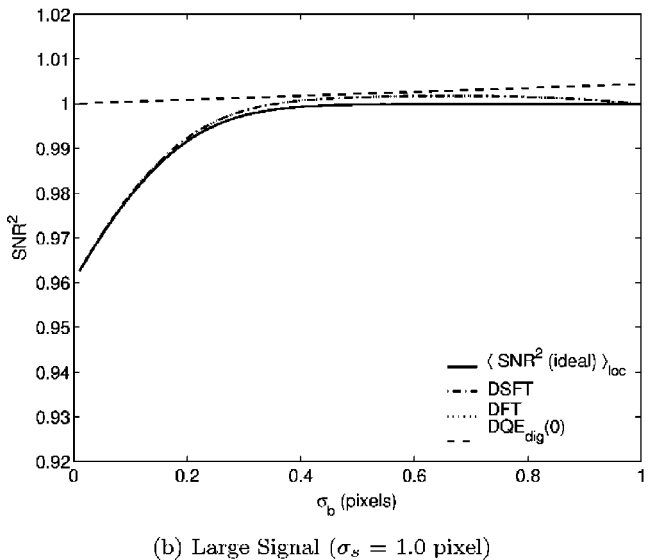
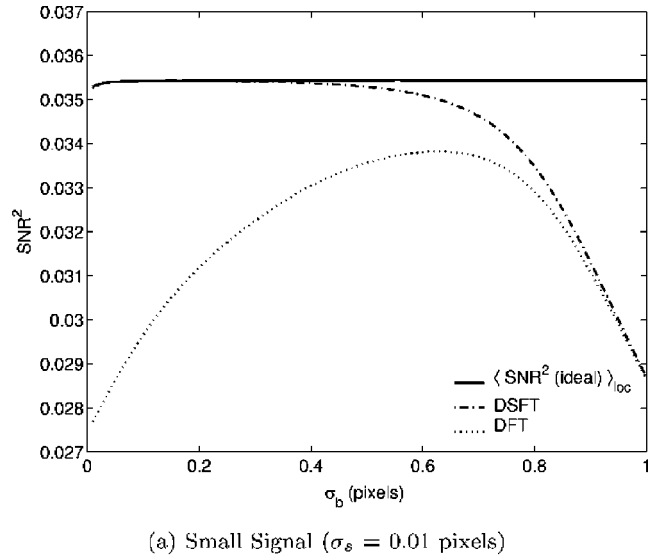


FIG. 5. SNR^2 vs presampling blur for (a) a small signal and (b) a large signal for the model with no electronic noise. The SNRs vary differently as we increase presampling blur (σ_b). The detectability is dominated by discretization effects which lead to a much larger decrease in detectability for small signals than for large signals. Note that the increase in $\text{DQE}_{\text{dig}}(0)$ is due to the finite detector size and that for the large signal, the DFT and DSFT plots lie on top of each other.

blur. The $\langle \text{SNR}^2(\text{ideal}) \rangle_{\text{loc}}$, on the other hand, remains constant.

As the signal size increases, the difference between the DSFT SNR and the DFT SNR decreases. This is because the frequency support of the signal mostly lies below half the sampling frequency of the detector. In that case, both SNRs are the same.

The $\text{DQE}_{\text{dig}}(0)$ is included in the plot not because it has been suggested as a figure of merit for evaluating presampling blur but because of its use as a summary measure for system characterization. As one would expect, $\text{DQE}_{\text{dig}}(0)$ changes very little with presampling blur. Blurring before detection should not change the total counts or the variance

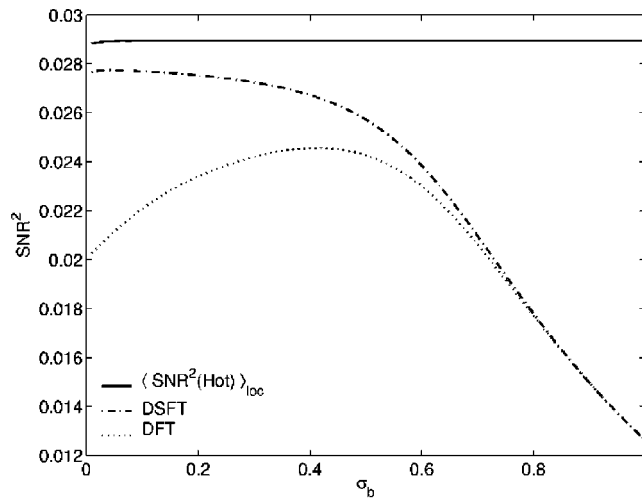
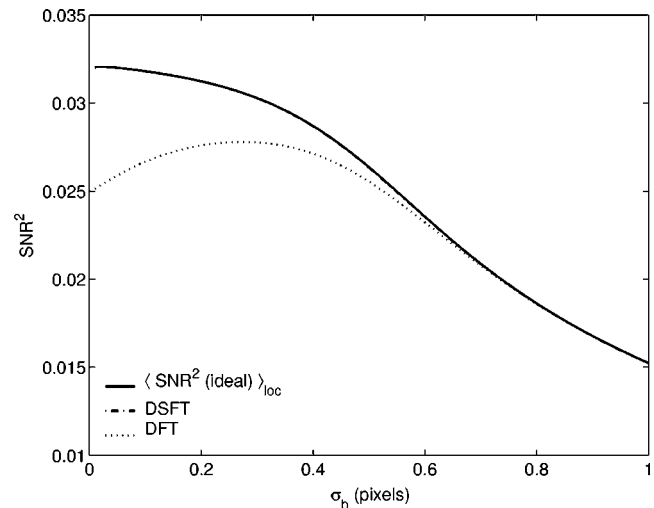
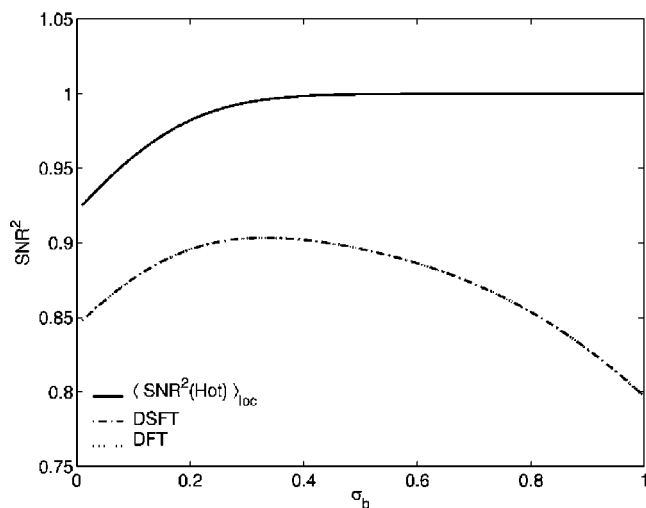
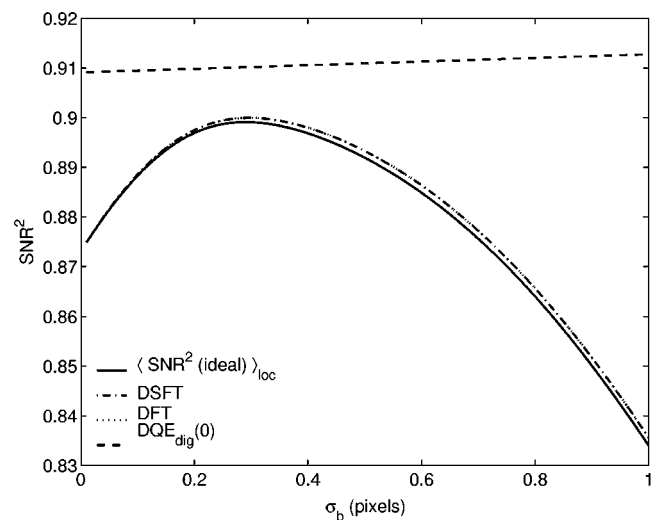
(a) Small Signal ($\sigma_s = 0.01$ pixels)(a) Small Signal ($\sigma_s = 0.01$ pixels)(b) Large Signal ($\sigma_s = 1.0$ pixel)(b) Large Signal ($\sigma_s = 1.0$ pixel)

FIG. 6. SNR^2 vs presampling blur for (a) a small signal and (b) a large signal for a detector with an interpixel gap=0.1 and no electronic noise. Surprisingly, $\langle \text{SNR}^2(\text{ideal}) \rangle_{\text{loc}}$ remains unchanged for the small signal. The decrease in detectability in the gap is compensated by an increase in the active part of the pixel. Note that for the large signal, the first three SNRs almost completely overlap.

FIG. 7. SNR^2 vs presampling blur for (a) a small signal and (b) a large signal for a detector with 10% electronic noise. We see an overall decrease in SNR but there are also fundamental changes in the behavior from the case with no electronic noise. The electronic noise washes out the maximum found in $\text{SNR}(\text{DFT})$ for small signals (Fig. 6). In Fig. 7, $\langle \text{SNR}^2(\text{ideal}) \rangle_{\text{loc}}$ and $\text{SNR}(\text{DSFT})$ lie on top of each other.

of the total counts. The increase that is seen with presampling blur is due to the errors in estimating the variance of the zero frequency with a finite size detector and DFT techniques. When we increase the detector size, the $\text{DQE}_{\text{dig}}(0)$ plot becomes flat.

Not only do the design decisions vary with the SNR chosen, they also vary with the signal of interest (Fig. 5). The design process has to include the signal of interest.

Introducing an interpixel gap produced an unexpected result in $\langle \text{SNR}^2(\text{ideal}) \rangle_{\text{loc}}$: it remained constant (see Fig. 6). Even though for a small amount of blur SNR for a small pixel at the gap is zero, SNR for the active part of the pixel increases such that SNR averaged over a pixel remains unchanged. The $\text{DQE}_{\text{dig}}(0)$ with no presampling blur is equal to the quantum efficiency (0.9) but as the blur increases the

effect of the gap is reduced. For large signals (Fig. 6) there is a small decrease in SNR due to the gap, but the qualitative behavior remains the same as in the case where there is no gap.

We also examined the effect of adding electronic noise to our model by adding independent Gaussian noise with 10% of the variance of the Poisson noise to our data. The results show that for small signals $\langle \text{SNR}^2(\text{ideal}) \rangle_{\text{loc}}$ no longer remains constant (Fig. 7). The ideal observer can undo the correlation arising from the presampling blur but not the variance from the electronic noise added after detection. For subpixel signals, we find that having no presampling blur is optimal. Even with electronic noise, for signals larger than a pixel, presampling blur increases detectability slightly

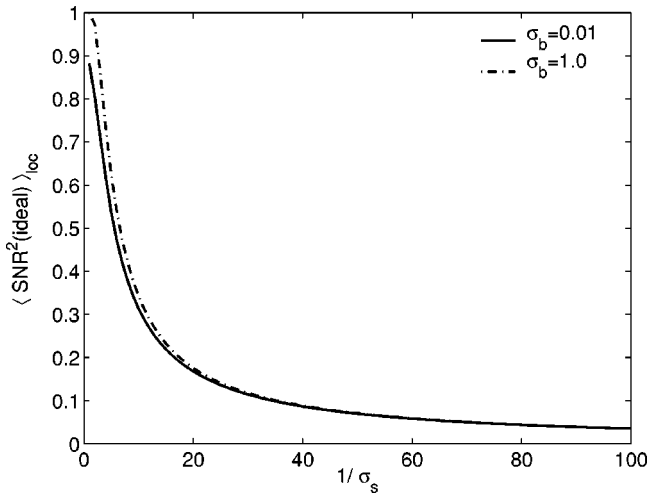


Fig. 8. $\langle \text{SNR}^2(\text{ideal}) \rangle_{\text{loc}}$ vs $1/\sigma_s$ for an interpixel gap of 0.1 pixels and no electronic noise. In this case, presampling blur helps to decrease the effect of the gap for all the signals studied.

($\sim 3\%$). We also see that introducing electronic noise after detection improves the approximation of the $\langle \text{SNR}^2(\text{ideal}) \rangle_{\text{loc}}$ by the DSFT SNR. Electronic noise makes the covariance matrix more diagonally dominant and hence closer to being diagonalized by the DFT. The $\text{DQE}_{\text{dig}}(0)$ is reduced as expected and does not change as we increase the presampling blur.

The NEQ_{dig} attempts to provide a scale-dependent figure of merit. A more theoretically sound approach is to plot $\langle \text{SNR}^2(\text{ideal}) \rangle_{\text{loc}}$ vs $1/\sigma_s$. This kind of a plot can be used to answer questions having to do with the size of a signal. Figure 8 shows how presampling blur helps to decrease the effect of the interpixel gap. If we add electronic noise, the presampling blur becomes undesirable (Fig. 9).

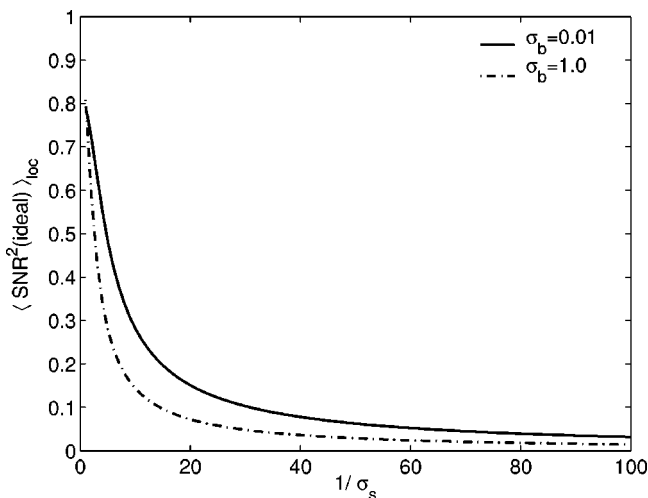


Fig. 9. $\langle \text{SNR}^2(\text{ideal}) \rangle_{\text{loc}}$ vs $1/\sigma_s$ for an interpixel gap of 0.1 pixels and 10% electronic noise.

VIII. DISCUSSION

The purpose of this paper was to explore the connection between the different formulations of NEQ_{dig} and the ideal SNR. In particular, we were interested in raising awareness of some of the limitations of commonly used Fourier methods. We are not claiming that there are no Fourier methods that could approximate the Hotelling detectability for the simple model used in this paper. As the reviewers pointed out, the use of a Hann window²⁵ for the estimation of the NPS_{dig} improves the correlation of the Fourier-based methods with Hotelling detectability. The details and representative results of this modification are included in Appendix B. The degree to which the Fourier approximations approach the Hotelling observer will depend on the size of the detector,¹⁷ the type of spectral estimation used,^{22,23,25} and the knowledge of the analytical model,^{13,21} among other factors.

What we found is that the NEQ_{dig} formulations studied here do not always correlate to detectability. For small signals, with and without electronic noise, $\text{SNR}(\text{DFT})$ has a maximum where $\text{SNR}(\text{ideal})$ remains constant or decreases. The design decision made by using $\text{SNR}(\text{DFT})$ would be different than the one taken if we look at signal detectability. Therefore, we should use a fully digital figure of merit that avoids the pitfalls that come from trying to combine continuous and discrete description of the imaging detector.

Our simple model only slightly tested the circulant nature of the data covariance matrix. In more realistic models, there will be more sources of error for these tasks.^{9,18} There are further complications with real measurements. The NPS is a stationary tool that is being applied to nonstationary detectors. While detectors have large numbers of pixels, smaller sections of the detector are used to estimate NPS_{dig} . The use of those smaller sections magnifies the errors associated with working in the frequency domain. In real data sets, there would also be errors associated with estimating the PSM_{TF} from the data.

The interpixel gap reveals a weakness in the location-averaged approach to detectability. Location averaging simplifies the analysis because it removes the location dependence for a flat background. This simplification carries with it the inability to distinguish between a detector with and without a pixel gap for a small signal. In the following paper,⁹ we will see that in structured backgrounds, location dependence cannot be avoided.

To obtain a figure of merit that depends on scale and takes into account measurement uncertainty without the use of Fourier methods, we suggest a plot of $\langle \text{SNR}^2(\text{ideal}) \rangle_{\text{loc}}$ as a function of signal size (Figs. 8–10). This pixel-domain quantification of system performance does not rely on shift-invariance or stationarity. Frequency is a natural surrogate for size in LSIV systems but in digital radiography it seems more natural to use signal size to talk about the scale dependence of a detector's performance. The normalization of the signals was done such that the $\text{SNR}_{\text{Hot}}^2$ could be interpreted as a DQE:

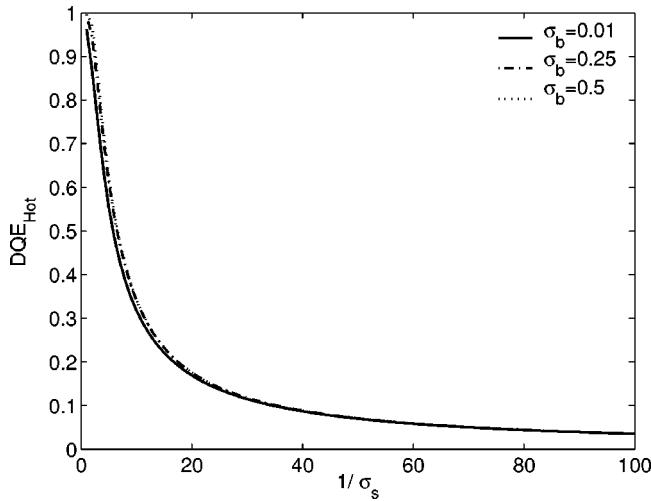


Fig. 10. DQE based on the Hotelling observer vs $1/\sigma_s$ for the same model as Fig. 2. Frequency is a surrogate for signal size in the same way that $1/\sigma_s$ is. This plot is a version of DQE that does not rely on Fourier methods but maintains all the properties of Fig. 2. The Hotelling DQE still shows improvement with increased presampling blur but much reduced from what Fig. 2 would imply.

$$\text{DQE}_{\text{Hot}} = \frac{\text{SNR}_{\text{Hot}}^2(\text{output})}{\text{SNR}_{\text{Hot}}^2(\text{input})}. \quad (54)$$

In Fig. 10, we plot the alternative formulation of DQE (DQE_{Hot}) in which there is little improvement by increasing presampling blur.

IX. CONCLUSIONS

The interpretation of DQE in terms of signal detectability for continuous data was established by Wagner.¹¹ This paper studies the connection between signal detectability and the commonly used extensions of DQE for digital detectors. We find that NEQ_{dig} and DQE_{dig} do not always correlate with signal detectability. These results encourage the verification of the assumptions made when using Fourier methods.

Working in the pixel domain avoids the stationarity and shift-invariance assumptions needed to justify NEQ_{dig} . Avoiding such assumptions makes the Hotelling-based SNR generalizable to more realistic situations.⁹ This generalizability and accuracy comes at the price of more computational expense and the necessity to include the signal in the evaluation process. To justify the added effort, we have shown that under some circumstances, using NEQ_{dig} -based figures of merit lead to the incorrect design decision. For the model used in this paper, the disagreement is restricted to extremely small lesions. As the model becomes more complicated,⁹ the effect affects larger lesions. If one adheres to the statistical-decision-theory interpretation of SNR, the SNR defined from the Hotelling observer provides the most reliable approach to system optimization. Ways to carry out these computations for large matrices and more realistic models is an active area of research.^{18,19} In the larger picture, both Fourier and pixel domain methods are trying to connect optimization of digital detectors to the detection task.^{18,19,21,24} We are interested in

encouraging the discussion about where Fourier methods have limitations and how can they be improved or replaced by pixel domain methods.

ACKNOWLEDGMENTS

The authors would like to thank K. J. Myers, E. Clarkson, and A. Lehovitch for stimulating discussions and helpful suggestions. This work was made possible by funding from NIH Grant Nos. RO1 CA52643 and P41 RR14304.

APPENDIX A

The DFT approach computes the presampling NEQ without the knowledge of the exact continuous presampling map. If we consider our model in the limit of an infinite detector with no electronic noise and $g_{\text{ps}}(x)$ restricted to be band-limited below half the sampling frequency, then $\hat{g}_{\text{ps}}(x) = g_{\text{ps}}(x)$. Sinc interpolation under those circumstances is an invertible transformation between the data and its continuous presampling representation. Since $\text{SNR}^2(\text{ideal})$ is invariant under invertible transformations, $\text{SNR}^2(\text{ideal})$ computed from the data is the same as the one computed before sampling:

$$\mathbf{g}_s^t \mathbf{K}_g^{-1} \mathbf{g}_s = \int_{-1/2}^{1/2} d\nu \frac{b_0^2 G_d^2 \text{PSMTF}^2(\nu)}{\text{NPS}_{\text{dig}}(\nu)} |S_0(\nu)|^2. \quad (\text{A1})$$

We quantify the errors incurred by these approximations by looking at the deviations between the DFT SNR and the ideal SNR. The largest deviations arise for small signals and small amounts of presampling blur. The errors are even larger when we include object variability.⁹

APPENDIX B

Tapering windows such as the Hann window²⁵ are sometimes used in spectral estimation to reduce spectral leakage. Multiplying the data vector (\mathbf{g}) by a window (a diagonal matrix, \mathbf{W}) that smoothly approaches zero at the edges reduces the effects of the finite sample size. We consider the Hann window,

$$W_{mm} = \frac{1}{2} \left(1 - \cos \left(2\pi \frac{m-1}{M} \right) \right). \quad (\text{B1})$$

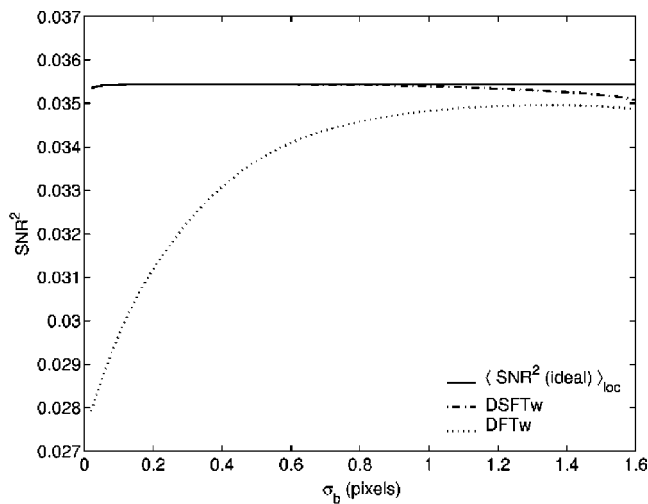
We can express the digital noise power spectra as

$$[\text{NPS}_{\text{dig}}]_m = \frac{1}{U} [\mathbf{D}\mathbf{W}\mathbf{K}_g\mathbf{W}^\dagger\mathbf{D}^\dagger]_{mm}, \quad (\text{B2})$$

with

$$U = \frac{1}{M} \sum_{m=1}^M W_{mm}^2. \quad (\text{B3})$$

We applied this window to our results. The use of the window had a significant effect. For our model, the use of the Hann window extended the blur range where Fourier methods correlated to the Hotelling detectability. Figure 11 reproduces Fig. 5 using a Hann window instead of the implicit



(a) Figure 5(a) using the Hann window

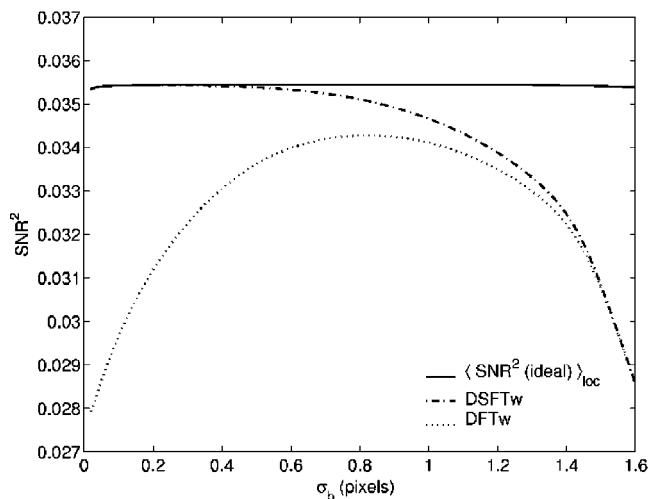
(b) Figure 5(a) using the Hann window and $M=64$

FIG. 11. We recomputed the plot from Fig. 5(a) using the Hann window for the estimation of the NPS_{dig} . In (a) we see a large effect in how the Fourier methods correlate with Hotelling detectability. Using $M=64$, (b) shows that the effect of the window will depend on the size of the images used. The “w” subscript means that the quantity was computed using the Hann window. Note that blur range is going up to 1.6

rect window. The Hann window decreases the effect of the finite detector size but the fundamental limitation remains. Figure 11 reproduces Fig. 5 using a Hann window but using images with $M=64$.

^{a)} Author to whom correspondence should be addressed; present address: Department of Radiology, Lucas MRS Center, Stanford University, Stanford, CA 94305-5488; electronic mail: pineda@stanford.edu

- ¹ I. Cunningham, “Applied Linear Systems Theory,” *Physics and Psychophysics*, Handbook of Medical Imaging, Vol. 1, edited by J. Beutel, H. L. Kundell, and R. L. Van Metter (SPIE, Bellingham, WA, 2000).
- ² M. L. Giger and K. Doi, “Investigation of basic imaging properties in digital radiography. 1. Modulation transfer function,” *Med. Phys.* **11**, 287–295 (1984).
- ³ M. L. Giger, K. Doi, and C. E. Metz, “Investigation of basic imaging properties in digital radiography. 2. Noise Wiener spectrum,” *Med. Phys.* **11**, 797–805 (1984).
- ⁴ J. T. Dobbins III, “Effects of undersampling on the proper interpretation of modulation transfer function, noise power spectra, and noise equivalent quanta of digital imaging systems,” *Med. Phys.* **22**, 171–181 (1995).
- ⁵ W. Zhao and J. A. Rowlands, “Digital radiology using active matrix readout of amorphous selenium: Theoretical analysis of detective quantum efficiency,” *Med. Phys.* **24**, 1819–1833 (1997).
- ⁶ J. A. Rowlands, W. G. Ji, W. Zhao, and D. L. Lee, “Direct conversion flat panel x-ray imaging: Reduction of noise by presampling filtration,” *Proc. SPIE* **3977**, 446–454 (2000).
- ⁷ R. F. Wagner and D. G. Brown, “Unified SNR analysis of medical imaging systems,” *Phys. Med. Biol.* **30**, 489–518 (1985).
- ⁸ H. H. Barrett, J. L. Denny, R. F. Wagner, and K. J. Myers, “Objective assessment of image quality. II. Fisher information, Fourier crosstalk, and figures of merit for task performance,” *J. Opt. Soc. Am. A* **12**, 834–852 (1995).
- ⁹ A. R. Pineda and H. H. Barrett, “Figures of merit for detectors in digital radiography. II. Finite number of secondaries and structured backgrounds,” *Med. Phys.* **31**, 359–367 (2004).
- ¹⁰ B. D. Gallas, “Signal detection in lumpy backgrounds,” Ph.D. dissertation, University of Arizona, Tucson, AZ, 2001.
- ¹¹ R. F. Wagner, “Decision theory and the detail signal-to-noise ratio of Otto Schade,” *Photograph. Sci. Eng.* **22**, 41–46 (1978).
- ¹² H. H. Barrett and K. J. Myers, *Foundations of Image Science* (Wiley, New York, 2004).
- ¹³ E. Clarkson, A. R. Pineda, and H. H. Barrett, “An analytical approximation to the Hotelling trace for digital x-ray detectors,” *Proc. SPIE* **4320**, 339–349 (2001).
- ¹⁴ H. L. Van Trees, *Detection, Estimation and Modulation Theory Pt. I* (Wiley, New York, 1968).
- ¹⁵ C. W. Helstrom, *Elements of Signal Detection & Estimation* (Prentice-Hall, Englewood Cliffs, NJ, 1995).
- ¹⁶ H. H. Barrett, C. K. Abbey, and E. Clarkson, “Objective assessment of image quality. III. ROC metrics, ideal observers, and likelihood-generating functions,” *J. Opt. Soc. Am. A* **15**, 1520–1535 (1998).
- ¹⁷ A. R. Pineda and H. H. Barrett, “What does DQE say about lesion detectability in digital radiography?,” *Proc. SPIE* **4320**, 561–569 (2001).
- ¹⁸ H. H. Barrett, K. J. Myers, B. Gallas, E. Clarkson, and H. Zhang, “Megalopiniakophobia: Its symptoms and cures,” *Proc. SPIE* **4320**, 299–307 (2001).
- ¹⁹ R. M. Gagne, J. S. Boswell, K. J. Myers, and G. Peter, “Signal detectability in digital radiography,” *Proc. SPIE* **4320**, 316–325 (2001).
- ²⁰ K. Fukunaga, *Introduction to Statistical Pattern Recognition* (Academic, Boca Raton, FL, 1972).
- ²¹ M. Albert and D. A. Maidment, “Linear response theory for detectors consisting of discrete arrays,” *Med. Phys.* **27**, 2417–2434 (2000).
- ²² A. Papoulis, *Probability, Random Variables, and Stochastic Processes* (McGraw-Hill, New York, 1991).
- ²³ S. L. Lawrence, *Digital Spectral Analysis with Applications* (Prentice-Hall, Englewood Cliffs, NJ, 1987).
- ²⁴ J. H. Siewerdsen and D. A. Jaffray, “Optimization of x-ray imaging geometry (with application to flat-panel cone-beam computed tomography),” *Med. Phys.* **27**, 1903–1914 (2000).
- ²⁵ A. V. Oppenheim, R. W. Schaffer, and J. R. Buck, *Discrete-Time Signal Processing* (Prentice-Hall, Englewood Cliffs, NJ, 1998).